J. Fluid Mech. (2004), *vol.* 508, *pp.* 23–44.
DOI: 10.1017/S0022112004008869 Printed in the United Kingdom

Effect of interstitial fluid on a granular flowing layer

By NITIN JAIN[1], J. M. OTTINO[1,2]† AND R. M. LUEPTOW[2]

[1]Department of Chemical Engineering, Northwestern University, Evanston, IL 60208, USA
[2]Department of Mechanical Engineering, Northwestern University, Evanston, IL 60208, USA

(Received 17 June 2003 and in revised form 23 September 2003)

A dominant aspect of granular flows is flow in thin surface layers. While an understanding of the dynamics of dry granular surface flow has begun to emerge, the case of flow when air is completely replaced by a liquid is largely unexplored. Experiments were performed using particle tracking velocimetry (PTV) in a quasi-two-dimensional rotating tumbler to measure the velocity field within the flowing layer of monodisperse spherical particles fully submerged in liquids, a granular slurry, for a range of Froude numbers, bead sizes, fluid densities and fluid viscosities. The thickness of the flowing layer and the angle of repose with a liquid interstitial fluid are generally larger than for the dry system under similar conditions, although the shear rate is generally smaller. The experimental measurements of shear rate match the theoretical predictions (dependent on the particle size, dynamic angle of repose, and static angle of repose) independent of the interstitial fluid. Furthermore, the velocity profiles for larger beads collapse independent of the interstitial fluid, while for smaller beads these profiles collapse on two distinct curves when using a scaling based on mass balance. However, a normalization based on the velocity of beads at the surface causes a collapse to a nearly linear velocity profile except where the velocity approaches zero logarithmically near the fixed bed, regardless of interstitial fluid. Likewise, the scaled number density profiles collapse, regardless of the interstitial fluid. The similarity in the flows of dry granular materials and granular materials submerged in liquids indicates that the physics of the flow is not strongly altered by the interstitial fluid.

1. Introduction

A fundamental understanding of granular flows is of critical importance for a number of industries – pharmaceuticals, polymers, ceramics, food processing, and others (Heywood 1999) – as well as for predictive geology. Until recently, only a relatively small number of attempts had been made to understand the flow, handling, and segregation of granular materials (Lacey 1954; Williams 1963; Bridgwater 1976). In the last few years, however, the number of papers published in this field has increased and considerable progress has been made (for summaries of recent work, see Duran 2000; Ristow 2000). Despite these efforts, our understanding of granular flow is still far less advanced than that of fluid flows, and a set of accepted general governing flow equations has not yet been developed for granular materials.

† Author to whom correspondence should be addressed: ottino@chem-eng.northwestern.edu.

The focus of this paper is to understand the effect of the interstitial fluid (air or liquid) on the flow of non-cohesive beads. We refer to the two situations as *dry*, where the interstitial fluid is air, and *slurry*, where the interstitial fluid is water or a glycerine–water mixture. The bulk of the granular flow dynamics literature addresses the case of dry materials, although there are some exceptions. There have been studies focusing on the effect of humidity or a fluid coating the particles, where the fraction of liquid in the system is less than a few per cent (Samadani & Kudrolli 2001; Li & McCarthy 2003; Tegzes, Vicsek & Schiffer 2003). These systems consist of three phases (granular solid, small quantities of a liquid, and a gas). As a result, the key physics is related to surface tension causing the granular particles to clump together. By contrast our system is a two-phase system (granular solid and a single fluid, either liquid or gas) and surface tension plays no role at all in our experiments, since there are no gas–liquid interfaces. Other studies have considered the formation of bands of particles in a horizontal rotating drum filled with a dilute suspension of particles (Boote & Thomas 1999; Tirumkudulu, Tripathi & Acrivos 1999) and the effect of an interstitial liquid on heaping (Medved, Jaeger & Nagel 2001). Finally, in the most closely related work to this study axial segregation of a slurry of beads of differing sizes in a half-filled long rotating drum was recently discovered (Jain *et al.* 2001; Fiedor & Ottino 2003). The rate of segregation is significantly faster for the case of a liquid interstitial fluid than for a gas.

Here, we study the granular flow in a quasi two-dimensional rotating tumbler half-filled with granular material and rotated about its axis, as shown in figure 1. This system has become a prototypical device to study mixing and segregation of granular matter. The simplicity of the system allows investigation of the dependence of the granular dynamics on the density and viscosity of the interstitial fluid.

When a horizontal circular tumbler partially filled with granular material is rotated about its axis, the material rotates as a solid body until it reaches its dynamic angle of repose. The flow inside a rotating tumbler can be divided into two parts: a bulk solid-body rotation undergoing a slow plastic deformation (Komatsu *et al.* 2001); and a thin flowing layer at the angled free surface. Depending on the speed of rotation, different flow regimes occur: avalanching, rolling or cascading; cataracting; and centrifuging (Henein, Brimacomble & Watkinson 1983; Rajchenbach 1990). This paper focuses exclusively on the rolling regime in which the flow is continuous and the upper surface of the flowing layer is nearly flat.

Most previous work on flow dynamics and segregation of granular materials in a rotating tumbler has been limited to dry granular materials. Nakagawa *et al.* (1993) conducted a detailed experimental study measuring the velocity of dry granular material in the flowing layer of a rotating tumbler using magnetic resonance imaging (MRI). They measured granular flow for particles of a single size and density at different angular velocities and found: (i) the velocity profile is approximately linear except near the interface between the layer and the bed; (ii) the velocity varies along the length of the layer with a maximum near the centre of the layer; and (iii) the number density of particles decreases across the flowing layer from the bed to the free surface. The granular flow dynamics in a quasi-two-dimensional rotating tumbler have also been measured using particle tracking velocimetry and high-speed digital photography. Jain, Ottino & Lueptow (2002) performed these measurements for a broad range of angular velocities, bead sizes, bead densities, and positions along the flowing layer. The results confirmed Nakagawa *et al.*'s findings and provided additional details: (i) the velocity profile is nearly linear in the upper three-quarters of the flowing layer, but the profile depends logarithmically on depth close to the

interface between the layer and 'fixed' bed; (ii) velocity profiles corresponding to different positions along the layer can be scaled using mass balance arguments; (iii) number density decreases dramatically in the upper half of the flowing layer, but is nearly uniform in the lower half of the layer. Furthermore, the velocity profiles were found to scale best with the surface velocity, and the number density profiles scaled quite well using geometric scaling rules. Bonamy, Daviaud & Laurent (2002) also found that the velocity profile is linear in the upper part of the flowing layer and logarithmically decreases close to the fixed bed for 3 mm steel beads.

Using conventional photography, Orpe & Khakhar (2001) measured the free surface profile and flowing layer thickness of dry beads in a quasi-two-dimensional circular tumbler at different particle diameter to tumbler radius ratios (d/L) and Froude numbers, $Fr = \omega^2 L/g$, where ω is the angular velocity of the tumbler and g is the acceleration due to gravity. They found that the scaled layer thickness (δ/L) increases with increasing Froude number or increasing d/L. In addition, they found that the scaled layer thickness and shape of the surface profiles are nearly identical when the Froude number and d/L are held constant, independent of the type of granular material. Ottino & Khakhar (2002) summarized the findings of these and other studies so that they can be applied to the design and scale up for problems of industrial importance.

With a few exceptions (e.g. Schleier-Smith & Stone 2001) there seems to be little fundamental work on the physics of granular flow under slurry conditions. In fact, the only related study of granular flow driven by tumbling with a liquid interstitial fluid seems to be our recent studies of granular segregation of glass particles of two different sizes in water-filled quasi-two-dimensional and three-dimensional circular tumblers (Jain *et al.* 2001; Fiedor & Ottino 2003). Both axial segregation (banding) and radial segregation occur in granular slurries, although the rate of formation of bands is considerably faster for the slurry condition compared to the dry condition. Theoretical understanding may not be completely lacking though. There is, in fact, more theoretical guidance available than can be gathered from the classical continuum descriptions of granular flow that go back to the work of Haff (1983) and others. In fact, recent work in suspensions of non-neutrally buoyant particles may yield considerable insight into this particular flow (Carpen & Brady 2002). As we shall show, a simple model based on a stress model assuming additivity of Coulombic and Bagnold stresses (Khakhar, Orpe & Ottino 2001*a*) captures some of the essential aspects of the results.

It should be noted also that although most studies of dry granular flow in a tumbler use the Froude number as the key dimensionless parameter, Klein & White (1988) proposed a dimensionless number of the form $g[(\rho_p - \rho)/\mu\omega^3]^{1/2}$ (referred to as the KW number later in this paper), where μ and ρ are the viscosity and density of the interstitial fluid, and ρ_p is the density of the granules. This dimensionless number has the advantage of including the nature of the interstitial fluid.

The focus of the present work is to measure quantitative differences in the granular flow dynamics for monodisperse dry and slurry systems. An estimate of the stresses involved is as follows. The typical stresses due to interparticle collisions are $\tau_c = \rho_p d^2 \dot{\gamma}^2$ (Bagnold 1954), whereas the stresses due to lubrication forces are $\tau_\mu = \mu\dot{\gamma}\, d/\varepsilon$ (Coussot & Ancey 1999), where $\dot{\gamma}$ is the shear rate and ε is the surface roughness. The ratio of interparticle collisional stresses to the lubrication stresses is the Bagnold number, $Ba = \tau_c/\tau_\mu = \dot{\gamma}\rho_p\, d\varepsilon/\mu$. For steel beads ($d \sim 3$ mm, $\rho_p \sim 7.5\,\mathrm{g\,cm^{-3}}$, $\varepsilon \sim 0.1\,\mu$m) tumbled in the rolling regime, the Bagnold number ranges from 10^0 for the dry case (air) to 10^{-2} for the slurry case (63% glycerine–water mixture, $\mu = 10.15$ cP).

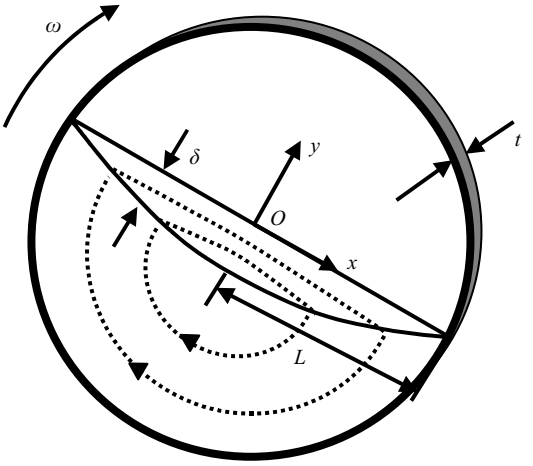

FIGURE 1. The rotating tumbler geometry with the coordinate system and the system parameters. Dotted curves indicate the paths of particles.

Based on this simple analysis, we might expect significant differences between the flow dynamics of dry material and a slurry.

This paper describes the dynamics of the flowing layer of a quasi-two-dimensional rotating drum for slurry systems with either water or mixtures of glycerine and water as the interstitial fluid. Using particle tracking velocimetry (PTV), we determine the profiles of streamwise velocity, granular temperature, number density and mass flux for flows in which the size of the granular particles, the rotational speed and the viscosity and density of interstitial fluid are varied. Our intent is to understand the relationship between particle interactions, as altered by the interstitial fluid, and macroscopic properties of the flowing layer. Where possible, results are compared with existing theory, although the effect of the interstitial fluid has not been explored in previous studies.

2. Experimental procedure

The circular tumbler used in the quasi-two-dimensional experiments is shown schematically in figure 1. The diameter of the tumbler ($2L$) was 28 cm. The back surface of the tumbler was a black-anodized aluminium plate to minimize electrostatic effects on the particles and optical noise effects in the digital images. The front faceplate was clear acrylic to permit optical access. A small hole in the front faceplate near the edge of the tumbler permitted liquid to be injected using a syringe, while another hole served as a vent. After filling the tumbler with the appropriate interstitial fluid, the holes were sealed. A stepper motor and micro series driver combination (SLO-SYN®) was used to rotate the tumbler at rotational speeds (ω) between 0.052 and 0.168 rad s^{-1}, corresponding to an order of magnitude change in Froude number, $0.39 \times 10^{-4} \leqslant Fr \leqslant 4.0 \times 10^{-4}$. Details of the experimental conditions are provided in table 1.

Spherical chrome steel beads (Fox Industries) with diameters (d) of 1.2 mm (1.16 ± 0.08), 2 mm (2.00 ± 0.04), and 3 mm (3.05 ± 0.06) were used for the experiments. The ratio between the tumbler radius and bead diameter varied from 47 to 117. Unlike our previous dry system measurements (Jain *et al.* 2002), glass beads were not used because the refractive index of glass is very close to that of water, making the

https://doi.org/10.1017/S0022112004008869 Published online by Cambridge University Press

Fluid	Viscosity (Pa s)	Kinematic viscosity ($m^2\,s^{-1}$)	d (mm)	ω ($rad\,s^{-1}$)	$Fr \times 10^4$	$KW \times 10^{-4}$	δ_0 (mm)	δ_0/d	β_m	$u_{surface}$ ($m\,s^{-1}$)	$\dot{\gamma}$ (s^{-1})
Air	1.85×10^{-5}	1.56×10^{-5}	1.16	0.052	0.39	1664	8.4	7.2	29.9	0.24	25.4
Air	1.85×10^{-5}	1.56×10^{-5}	1.16	0.094	1.26	685	11.2	9.7	32.6	0.62	48.2
Air	1.85×10^{-5}	1.56×10^{-5}	1.16	0.168	4.03	287	14	12.1	34.1	0.77	56.1
Air	1.85×10^{-5}	1.56×10^{-5}	2	0.052	0.39	1664	12.6	6.3	26.6	0.17	11.8
Air	1.85×10^{-5}	1.56×10^{-5}	2	0.094	1.26	685	14	7.0	28.8	0.27	19.5
Air	1.85×10^{-5}	1.56×10^{-5}	2	0.168	4.03	287	16.1	8.1	30.3	0.50	30.9
Air	1.85×10^{-5}	1.56×10^{-5}	3	0.052	0.39	1664	15.4	5.1	24.6	0.11	6.7
Air	1.85×10^{-5}	1.56×10^{-5}	3	0.094	1.26	685	18.9	6.3	26.6	0.14	7.6
Air	1.85×10^{-5}	1.56×10^{-5}	3	0.168	4.03	287	19.6	6.5	27.5	0.24	12.5
Water	1.00×10^{-3}	1.00×10^{-6}	1.16	0.052	0.39	211	9.8	8.4	33.0	0.19	19.8
Water	1.00×10^{-3}	1.00×10^{-6}	1.16	0.094	1.26	87	11.9	10.3	34.0	0.34	27.6
Water	1.00×10^{-3}	1.00×10^{-6}	1.16	0.168	4.03	36	12.6	10.9	35.8	0.44	35.9
Water	1.00×10^{-3}	1.00×10^{-6}	2	0.052	0.39	211	14	7.0	30.5	0.12	7.7
Water	1.00×10^{-3}	1.00×10^{-6}	2	0.094	1.26	87	16.1	8.1	31.7	0.21	12.0
Water	1.00×10^{-3}	1.00×10^{-6}	2	0.168	4.03	36	18.2	9.1	33.0	0.35	20.7
Water	1.00×10^{-3}	1.00×10^{-6}	3	0.052	0.39	211	14.7	4.9	29.7	0.13	7.7
Water	1.00×10^{-3}	1.00×10^{-6}	3	0.094	1.26	87	16.8	5.6	31.0	0.20	10.5
Water	1.00×10^{-3}	1.00×10^{-6}	3	0.168	4.03	36	19.6	6.5	31.7	0.28	13.4
Glycerine	2.89×10^{-3}	2.65×10^{-6}	3	0.052	0.39	123	15.4	5.1	29.7	0.12	7.5
Glycerine	2.89×10^{-3}	2.65×10^{-6}	3	0.094	1.26	51	16.1	5.4	30.1	0.17	11.6
Glycerine	2.89×10^{-3}	2.65×10^{-6}	3	0.168	4.03	21	17.5	5.8	31.8	0.28	16.1
Glycerine	6.79×10^{-3}	5.96×10^{-6}	3	0.052	0.39	80	17.5	5.8	31.0	0.10	6.2
Glycerine	6.79×10^{-3}	5.96×10^{-6}	3	0.094	1.26	33	18.2	6.1	31.8	0.17	9.7
Glycerine	6.79×10^{-3}	5.96×10^{-6}	3	0.168	4.03	14	19.6	6.5	32.2	0.24	12.8
Glycerine	1.02×10^{-2}	8.73×10^{-6}	3	0.052	0.39	65	16.1	5.4	31.4	0.10	6.3
Glycerine	1.02×10^{-2}	8.73×10^{-6}	3	0.094	1.26	27	17.5	5.8	32.2	0.13	8.3
Glycerine	1.02×10^{-2}	8.73×10^{-6}	3	0.168	4.03	11	22.4	7.5	32.6	0.22	10.5

TABLE 1. Key parameters and resulting characteristics of the flowing layer.

	Density ($kg\,m^{-3}$)	Viscosity (Pa s)	Kinematic viscosity ($m^2\,s^{-1}$)	Bagnold number
Air	1.184	1.85×10^{-5}	1.56×10^{-5}	6.95
Water	999	1.00×10^{-3}	1.00×10^{-6}	0.13
38% Glycerine	1094	2.89×10^{-3}	2.65×10^{-6}	0.04
56% Glycerine	1144	6.79×10^{-3}	5.96×10^{-6}	0.02
63% Glycerine	1163	1.02×10^{-2}	8.73×10^{-6}	0.01

TABLE 2. Fluid properties and Bagnold number for 3 mm beads in the various interstitial fluids at 25 °C.

beads much harder to image. The selection of steel beads over glass beads for the experiments has been shown to have no impact on the shape and scaling of the velocity profiles (Jain *et al.* 2002). In all experiments, the dimensionless thickness of the tumbler was set to 3.2–3.4 times the diameter of the beads by changing the axial length t of the tumbler to maintain similarity with respect to particle diameter. Results are undoubtedly dependent on t. However, an order of magnitude analysis shows that the wall effects are relatively small (Khakhar *et al.* 2001*b*). In addition, Orpe & Khakhar (2001) in a series of extensive experiments, considered a range of cylinder lengths and particle diameters as well as Froude numbers. Their results showed that the flow is relatively unaffected by the sidewalls for small values of d/L. Furthermore, our previous dry experiments with glass beads of similar sizes in the same tumbler suggest a negligible impact of tumbler thickness on the velocity profiles (Jain *et al.* 2002). The filling fraction was 50% for all the experiments, and all of the measurements were made at the centre of the length of the flowing layer.

In all of the slurry experiments, the tumbler was completely filled with the interstitial liquid. Most experiments were done with air or pure water as the interstitial fluid. In addition, several experiments were performed with a mixture of water and glycerine providing a range of densities and viscosities indicated in table 2. These viscosities were measured using a falling ball viscometer (Gilmont Instruments) at 25 °C. The density was measured using a hydrometer.

Several techniques have been used to measure the granular flow including MRI (Nakagawa *et al.* 1993), X-ray imaging (Baxter *et al.* 1989), radioactive tracers (Harwood 1977), and layering of granules of different colours (Takahashi, Suzuki & Tanaka 1968). In this work, we use imaging techniques based on particle image velocimetry (PIV) and PTV, which have provided measurements of the velocity in dry granular flow with high spatial and temporal resolution (Warr, Jacques & Huntley 1994; Medina *et al.* 1998; Lueptow, Akonur & Shinbrot 2000; Bonamy *et al.* 2002; Jain *et al.* 2002).

The clear side of the tumbler was illuminated by a dual-YAG laser system in a back-scatter mode. The cylindrical laser beam passed through a diffuser plate to generate a flash of light. The light reflected back from the particles in the tumbler was recorded by a standard PIV system having a CCD camera with a resolution of 1016×1000 pixels. The camera's field of view was zoomed in on the centre of the lens shaped layer (figure 1) to capture a region about 3 cm square, corresponding to 8–20 particle diameters. The PIV system (TSI Inc.) synchronized the camera, laser flashes and frame grabber to obtain a pair of images separated by a small time delay ($\Delta t \sim O(10^{-3})$ s) at a frequency of 15 Hz. PIV was used to estimate the velocity of

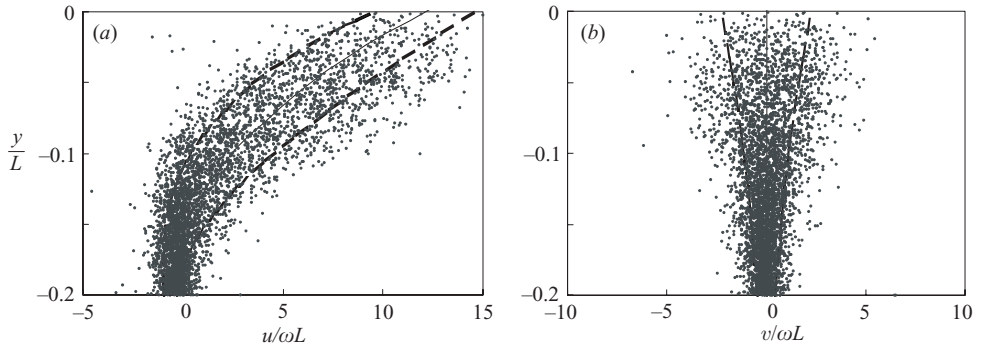

FIGURE 2. Scatter plot of velocities a function of depth (y) at $x = 0$ for 3 mm steel beads with water as the interstitial fluid and at $Fr = 4.03 \times 10^{-4}$. (a) Streamwise velocity (u); the solid curve is a third order polynomial fit through the data. (b) Transverse velocity (v); the solid line is at $v = 0$. The dashed curves on either side of the solid curve correspond to one standard deviation.

particles on a statistically averaged basis, followed by PTV that was used to find the particle velocity on a particle-by-particle basis (Cowen & Monismith 1997; Jain *et al.* 2002). Typically, 99 image pairs were obtained over several seconds. Since the velocity was much higher at the surface of the flowing layer than at the interface between the layer and the bed, two different time delays (Δt) were used for each experimental condition and the results were overlaid to provide adequate resolution of the displacement through the entire depth of the flowing layer. We estimate the error in the velocity measurement of a single particle to be less than 2%, based on the spatial and temporal resolution of the PTV system.

To obtain the velocity profile in the flowing layer, the displacements of the particles in a narrow strip about 3 particles wide in the streamwise x-direction and extending into the fixed bed in the transverse y-direction at the centre of the drum ($x = 0$) were collected from all 198 image pairs (99 image pairs at each of two delays between images). The delay between image pairs was long enough so that the same particles did not appear in the narrow strip for consecutive image pairs. Figure 2 shows an example of streamwise (u) and transverse (v) velocity for 3 mm steel beads rotated at $Fr = 4.03 \times 10^{-4}$, with water as the interstitial fluid. There are approximately 10 000 data points in the figure, with each data point corresponding to the velocity of an individual bead. The velocity profiles are non-dimensionalized by the angular velocity and radius of the tumbler and are plotted in the traditional boundary layer format ($y/L = 0$ is the surface of the flowing layer). The solid curves represent the average velocity profile and the dashed curves represent one standard deviation from the average profile. The streamwise velocity is maximum at the surface of the flowing layer and smoothly decreases to zero moving toward the fixed bed. The average transverse velocity is zero, because at the centre of the layer there is no flux in the y-direction (material neither enters nor leaves the layer). Since all of our experiments were performed at the centre of the layer, we focus our attention on the streamwise velocity.

Key to many of the results presented here is the accurate measurement of the thickness of the flowing layer δ_0, where the subscript indicates that the measurement is at $x = 0$. To determine δ_0, the flowing layer was subdivided into 20 bins, so that the average streamwise velocity in the bin nearest the fixed bed had a zero or slightly negative value, while all other bins were positive. The method required starting with

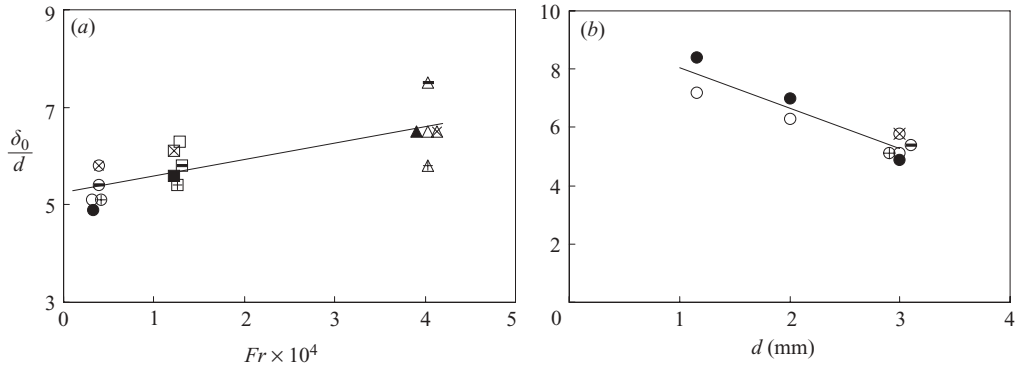

FIGURE 3. Dependence of dimensionless flowing layer thickness on (*a*) Froude number for 3 mm steel beads and (*b*) bead size for $Fr = 0.39 \times 10^{-4}$. Symbols: ●, $Fr = 0.39 \times 10^{-4}$; ■, $Fr = 1.26 \times 10^{-4}$; ▲, $Fr = 4.03 \times 10^{-4}$. Symbol fill: open, air; black, water; open with a '+' in the middle, 38% glycerine; open with a '×' in the middle, 56% glycerine; and open with a horizontal line, 63% glycerine. In some cases, data points that would overlay one another are shifted horizontally by a small amount to make all data points visible.

an approximation for δ_0 and then varying δ_0 slightly to obtain a zero or negative velocity in the last bin.

3. Results

We first consider the nature of the flowing layer in terms of its thickness, δ_0, and its dynamic angle of repose, β_m, both of which are commonly measured quantities in granular flowing layers and are characteristics of the flow. Results are indicated in table 1. The flowing layer is only several particle diameters thick, with δ_0/d ranging from 4.9 to 12.1 over all bead diameters and interstitial fluids. For comparison, Felix, Falk & D'ortona (2002) found $7.1 \leqslant \delta_0/d \leqslant 11.7$ for 1–1.4 mm glass beads in air, which is very similar to our measured layer thickness of $7.2 \leqslant \delta_0/d \leqslant 12.1$ for 1.2 mm steel beads in our slightly larger tumbler. The dimensionless layer thickness δ_0/d increases with increasing Froude number for any particular bead size and interstitial fluid, as indicated in table 1. If we consider only 3 mm beads, for which we have measurements over a wide range of interstitial fluid viscosities, the flowing layer thickness increases with Froude number, as shown in figure 3(*a*), consistent with previous results (Nakagawa *et al.* 1993; Boateng & Barr 1997; Orpe & Khakhar 2001). What is more interesting is that the thickness of the flowing layer is essentially independent of the interstitial fluid, even though the absolute viscosity and fluid density vary by three orders of magnitude and the kinematic viscosity varies by a factor of 15.6, as indicated in table 2. Similar results are evident in table 1 for smaller bead sizes.

If the Froude number is held constant, the data in table 1 indicate that the dimensional flowing layer thickness δ_0 increases with bead size, but the dimensionless flowing layer thickness, δ_0/d, decreases with bead size, as shown in figure 3(*b*) for the lowest Froude number. Again, the result is essentially independent of the interstitial fluid. Finally, as is evident in table 1, plotting either δ_0 or δ_0/d versus the KW number does not show any discernable trend. Thus, it appears that this scaling does not adequately account for the influence of the interstitial fluid on the thickness of the flowing layer. The reason for this may be related to the length scale. The inverse

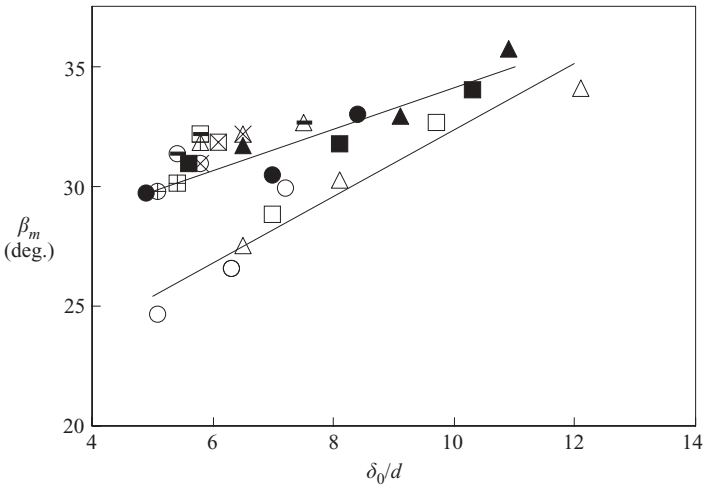

FIGURE 4. Relationship between the angle of repose and the thickness of the flowing layer for all the 27 experimental cases. Two different relations result for dry and slurry systems, as indicated by the least-square fits to the data. Symbols: ●, $Fr = 0.39 \times 10^{-4}$; ■, $Fr = 1.26 \times 10^{-4}$; ▲, $Fr = 4.03 \times 10^{-4}$. Symbol fill: open, air; black, water; open with a '+' in the middle, 38% glycerine; open with a '×' in the middle, 56% glycerine; and open with a horizontal line, 63% glycerine.

KW number, $(\mu\omega^3)^{1/2}/(\rho_p - \rho)^{1/2}g$, can be written in a form similar to the Froude number. In this form the resulting length scale is $[\mu/\omega(\rho_p - \rho)]^{1/2}$, which is a viscous length scale. Apparently, the kinematics related to the drum geometry (length scale L) drive the flow rather than the viscous interactions between particles.

The dynamic angle of repose (β_m) was measured by superimposing the 99 image pairs captured for PIV and drawing a line adjacent to the topmost particles. The results in table 1 indicate that β_m varies from 24.6° to 35.8° over the entire range of bead sizes, Froude numbers and interstitial fluids. The angle of repose increases with increasing Froude number for any specific particle diameter and interstitial fluid consistent with previous results (DasGupta, Khakhar & Bhatia 1991; Hill & Kakalios 1994; Dury *et al.* 1998; Orpe & Khakhar 2001). Orpe & Khakhar (2001) reported that the angle of repose in air for 2 mm steel beads increases from approximately 25° to 40° for $0 \leqslant Fr \leqslant 25 \times 10^{-4}$ in a 32 cm diameter tumbler. Our data for the same size beads in air at the low end of this range of Froude numbers ($0.39 \times 10^{-4} \leqslant Fr \leqslant 4.0 \times 10^{-4}$) show consistent results (table 1), with the angle of repose increasing from 26.6° to 30.3°.

For a specific Froude number and interstitial fluid, the angle of repose decreases as the beads become larger, consistent with previous results (DasGupta *et al.* 1991; Dury & Ristow 1997). The angle of repose is consistently higher for a liquid interstitial fluid than for air as the interstitial fluid for a given particle size and Froude number, as indicated in table 1. The angle of repose increases slightly as the viscosity increases for liquid interstitial fluids, perhaps related to the increased hydrodynamic shear force as one particle slides past another. The angle of repose is linearly related to the thickness of the flowing layer, as shown in figure 4. At higher Froude numbers, the flowing layer is more dilated and therefore thicker, leading to a higher angle of repose (Reynolds 1885; Duran 2000). Furthermore, it is clear that the linear relation between the angle of repose and flowing layer thickness is different for the dry system

and the slurry system, as indicated in figure 4. Of course, particles interact via direct contact in a dry system, but interact via a thin liquid layer when an interstitial liquid is present. Lubrication forces play a role below some length scale related to the size of the asperities on the surface of the particle. That the hydrodynamic lubrication between particles in a liquid alters the angle of repose of the flowing layer is not surprising given that the angle of repose is generally thought to be related to the friction between particles (Duran 2000). This result differs from that for a sandpile, where the angle of repose for dry flow and slurries was similar (Samadani & Kudrolli 2001). However, the difference may be a consequence of different flow geometries (sandpile versus tumbler) or that the flowing layer thickness is such that there is little difference in the angle of repose for different fluids (large δ_0/d in figure 4).

An important issue for continuum dynamic simulations is a scaling law for the velocity profile independent of the bead size, Froude number and interstitial fluid. Two different methods have been used to scale streamwise velocity profile (Jain *et al.* 2002). The first method results from equating mass flow rate in the flowing layer to the mass flow rate in the fixed bed, so that to a first approximation

$$u_{av} = \omega L^2/2\delta_0, \tag{1}$$

where u_{av} is the average velocity in the flowing layer. Based on this relation, the velocity should be scaled as $u\delta_0/\omega L^2$. In the second method, the streamwise velocity profile is simply scaled using the maximum streamwise velocity $u_{surface}$ that occurs at the surface of the flowing layer. Values for $u_{surface}$ are indicated in table 1.

The average streamwise velocity is plotted using the mass balance scaling in figure 5(*a*) for 3 mm beads in air, water and glycerine–water mixtures at three different Froude numbers (15 experimental velocity profiles). The mass balance scaling collapses the data well, suggesting that changing the interstitial fluid leads to no significant change in the dynamics of the flowing layer. This is particularly surprising given the wide range of viscosity and density. The dynamic viscosity and density each vary by three orders of magnitude, and the kinematic viscosity varies by a factor of 15.6, as indicated in table 2. Furthermore, the collapse is noteworthy considering the broad range of Bagnold numbers for the different interstitial fluids. To determine the Bagnold number, the characteristic shear rate was estimated as $(g/d)^{1/2}$. For air, the Bagnold number is approximately 7, while for the 63% glycerine–water mixture, the Bagnold number is 0.013. The fact that data collapses over such a wide range of Bagnold numbers suggests that the interaction between particles may not be properly characterized by the Bagnold number. In a recent critical review of Bagnold's (1954) suspension experiments, evidence is provided that Bagnold's results were affected by the experimental apparatus, a short Taylor–Couette cell (Hunt *et al.* 2002). This recent result together with our results that the Bagnold number does not characterize the effect of the interstitial fluid suggest that the Bagnold number should be used with care.

The streamwise velocity does not collapse as well for 2 mm steel beads with water and air as the interstitial fluids, as shown in figure 5(*b*). There is a reasonable collapse between the velocity profiles for dry and slurry conditions in the lower half of the layer. However, in the top half of the flowing layer, dry beads move a little faster than the beads in water. For 1.2 mm steel beads, there are two velocity profiles, as shown in figure 5(*c*), with the dry beads at the lowest Froude number falling on the same profile as the beads in water for all Froude numbers, while the dry beads at the higher Froude numbers fall on a different profile.

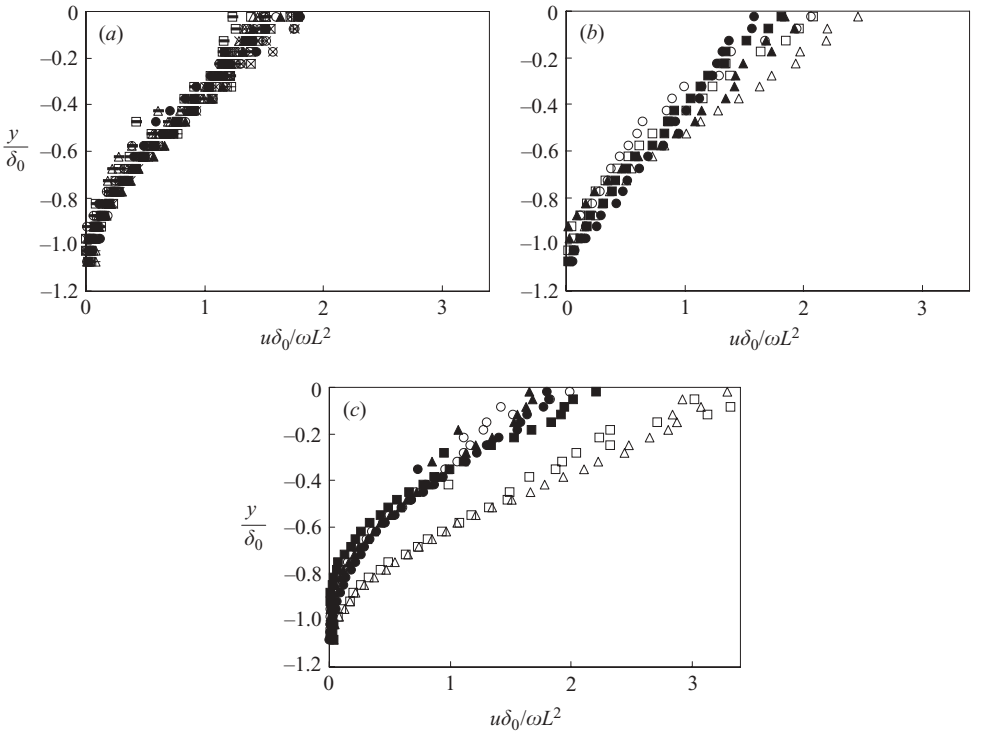

FIGURE 5. Scaled streamwise velocity profile at $x = 0$. (*a*) 3 mm beads; (*b*) 2 mm beads; (*c*) 1.2 mm beads. Symbols: ●, $Fr = 0.39 \times 10^{-4}$; ■, $Fr = 1.26 \times 10^{-4}$; ▲, $Fr = 4.03 \times 10^{-4}$. Symbol fill: open, air; black, water; open with a '+' in the middle, 38% glycerine; open with a '×' in the middle, 56% glycerine; and open with a horizontal line, 63% glycerine.

The velocity profiles for three different bead sizes, three rotational speeds, and interstitial fluids ranging from air to glycerine–water mixtures (27 cases) are overlaid in figure 6(*a*). The velocity profiles for the slurry systems at all Froude numbers and for the dry system at the lowest Froude number are similar, while the velocity profiles for the smallest beads in the dry system at the two higher Froude numbers have substantially different profiles. Clearly, a scaling based on mass balance arguments does not collapse the data. A similar puzzling result of different velocity profiles for smaller beads at higher Froude numbers has been observed for dry systems of glass beads (Jain *et al.* 2002). While we do not have any explanation to offer, this is undoubtedly due to the interplay between frictional, collisional, and viscous forces.

Figure 6(*b*) uses the alternative scheme for the velocity profile based on normalizing the streamwise velocity with the velocity at the top of the flowing surface, $u_{surface}$. While this is a normalization not a physically based scaling, it is useful to show the similarity in the shape of the velocity profiles. This normalization is not unlike using the free-stream velocity and boundary-layer thickness in plotting turbulent boundary-layer velocity profiles. An important conclusion that can be drawn from figure 6(*b*) is that the streamwise velocity profile is approximately linear for most of the flowing layer from the top of the flowing surface to a depth of $y/\delta_0 \sim -0.75$, as indicated by the solid line sketched through the data. In this region the streamwise velocity can be approximated as

$$u/u_{surface} \approx 1 + 1.2(y/\delta_0). \tag{2}$$

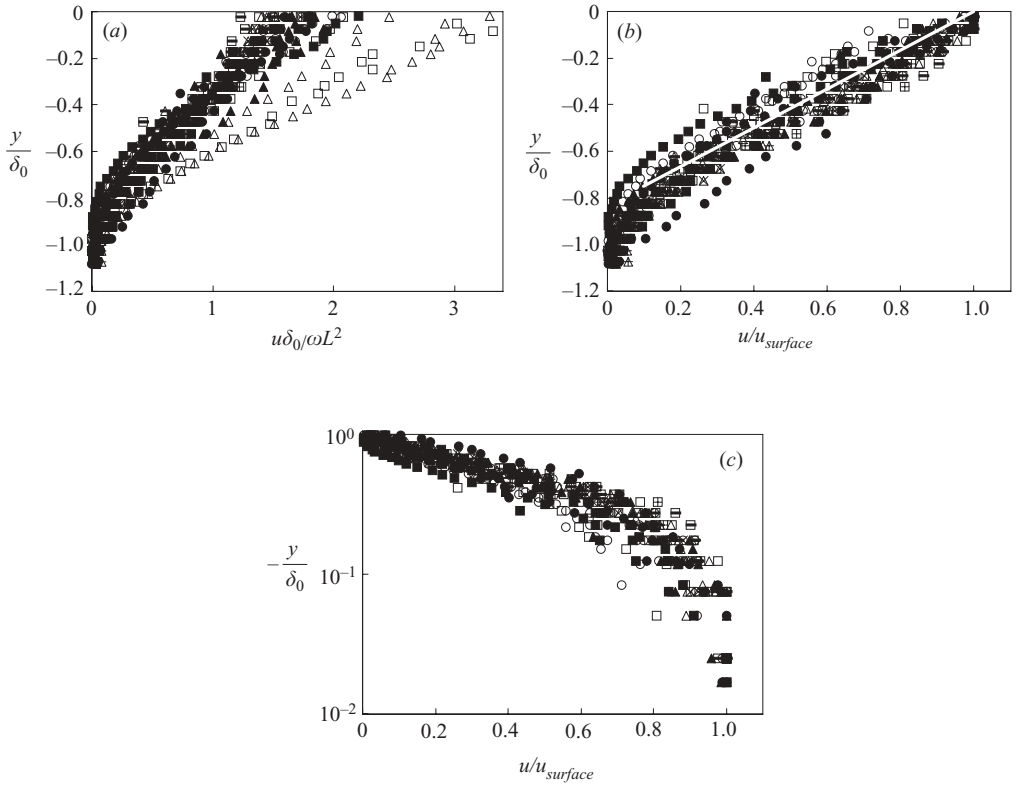

FIGURE 6. Streamwise velocity profile at $x = 0$ for 27 cases. (*a*) Scaling of velocity based on mass balance arguments; (*b*) velocity normalized by the velocity at the surface of the flowing layer, $u_{surface}$; (*c*) velocity normalized by the velocity at the surface of the flowing layer, $u_{surface}$ plotted on a semi-log scale. Symbols: ●, $Fr = 0.39 \times 10^{-4}$; ■, $Fr = 1.26 \times 10^{-4}$; ▲, $Fr = 4.03 \times 10^{-4}$. Symbol fill: open, air; black, water; open with a '+' in the middle, 38% glycerine; open with a '×' in the middle, 56% glycerine; and open with a horizontal line, 63% glycerine.

This relation is independent of the interstitial fluid. Below the linear region, the streamwise velocity smoothly decreases to zero approaching the fixed bed.

Figure 6(*c*) shows the same data as in figure 6(*b*), except plotted using semi-log coordinates. This provides an insight into the nature of the velocity profile near the interface between the flowing layer and fixed bed (at $y/\delta_0 = -1$). In the cases of both dry and slurry systems, the velocity profiles logarithmically approach zero at the fixed bed, consistent with previous results for dry glass beads (Jain *et al.* 2002). These results support the concept suggested by Komatsu *et al.* (2001) for flow down a granular pile that even in the 'fixed bed' there exists creep flow consisting of slow rearrangements of particles. However, our results cannot be compared directly to those of Komatsu *et al.* They found an exponential decay of velocity with depth *below* the flowing layer, whereas our results indicate a logarithmic dependence of velocity on depth in the flowing layer just *above* the 'fixed bed'. Of course, the precise location of the boundary between the flowing layer and the 'fixed bed' is difficult to define, particularly in light of the slow particle rearrangements in the fixed bed. Nevertheless, our results very near the lower bound of the flowing layer are consistent with the creep velocity suggested by Komatsu *et al.*

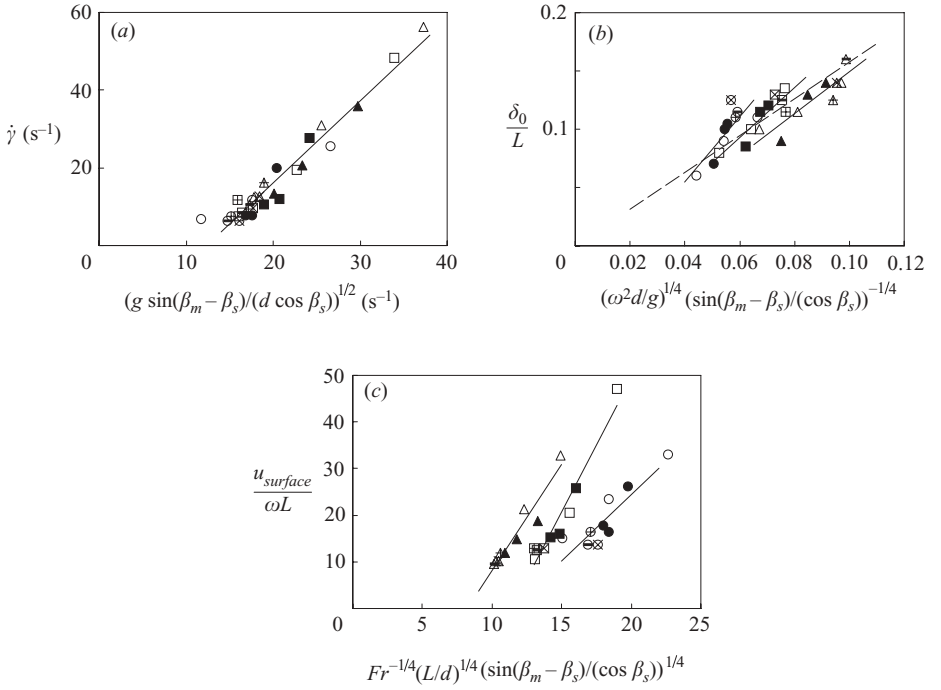

FIGURE 7. Experimentally measured characteristics of the flowing layer are compared to the theoretically predicted values. (*a*) Shear rate. (*b*) Flowing layer thickness. (*c*) Surface velocity. Symbols: ●, $Fr = 0.39 \times 10^{-4}$; ■, $Fr = 1.26 \times 10^{-4}$; ▲, $Fr = 4.03 \times 10^{-4}$. Symbol fill: open, air; black, water; open with a '+' in the middle, 38% glycerine; open with a '×' in the middle, 56% glycerine; and open with a horizontal line, 63% glycerine.

The experimental shear rate $\dot{\gamma}_0$, was calculated by fitting a line to the linear portion of each individual velocity profile. Results are shown in table 1. The shear rate ranges from a minimum of 6.2 s^{-1} (for 3 mm beads in 56% glycerine–water mixture) to a maximum of 56.1 s^{-1} (for 1.2 mm beads in air). The shear rate increases with an increase in the Froude number for any bead diameter and interstitial fluid, as would be expected. However, for any fixed Froude number and interstitial fluid, the shear rate decreases as the bead diameter increases. This is a direct result of the decrease in the surface velocity and the increase in the thickness of the flowing layer (δ_0) as the bead size increases. For 1.2 mm and 2 mm beads, the shear rate is higher for the dry case than for the slurry case. However, the opposite is true for 3 mm beads, primarily because the surface velocity is greater in the slurry than for dry beads.

Khakhar *et al.* (2001*a*) predicted that the shear rate should be given by:

$$\dot{\gamma}_{theor} \approx \left[\frac{g}{d}\frac{\sin(\beta_m - \beta_s)}{\cos \beta_s}\right]^{1/2}, \tag{3}$$

where, β_s is the static angle of repose. At the end of every experimental run, the motor was turned off and a digital picture was taken for measurement of β_s. The procedure to measure β_s was similar to that for measuring dynamic angle of repose (β_m). Figure 7(*a*) compares the experimentally-measured shear rate for all bead sizes, Froude numbers, and interstitial fluids with the theoretical shear rate. The relationship between the theoretical estimate of the shear rate and the measured shear rate holds

regardless of the interstitial fluid properties. For this data set, the exact relation is

$$\dot{\gamma} = 2.1\left[\frac{g\sin(\beta_m - \beta_s)}{d\cos\beta_s}\right]^{1/2} - 26. \tag{4}$$

Khakhar *et al.* (2001*a*) also showed that the shear rate can be used to estimate the thickness of the flowing layer. Since the velocity profile is approximately linear, the shear rate can be approximated as:

$$\dot{\gamma} \approx 2u_{av}/\delta_0, \tag{5}$$

which together with (1) leads to:

$$\delta_0/L = (\omega/\dot{\gamma})^{1/2}. \tag{6}$$

Combining the expression for shear rate (equation (3)) with (6) leads to a theoretical value for the flowing layer thickness that is based on the particle diameter, angular velocity, radius of the tumbler and angle of repose.

$$\left.\frac{\delta_0}{L}\right|_{theor} \approx \left(\frac{\omega^2 d}{g}\right)^{1/4}\left[\frac{\sin(\beta_m - \beta_s)}{\cos\beta_s}\right]^{-1/4}. \tag{7}$$

The measured layer thickness is clearly related to this theoretical value as shown in figure 7(*b*). In some sense, this figure is just the data in figure 4 replotted in a different format. However, the dashed line indicating the least-squares fit for all the data, shows that this simple theoretical prediction is accurate to within a multiplicative factor of $O(1)$, independent of the interstitial fluid, Froude number, or bead size. Considering only a single Froude number (e.g. just the circular symbols) a slightly different linear relation between the measured and theoretical values results, as indicated by the nearly parallel solid lines in figure 7(*b*). This suggests that while the prediction of (7) works fairly well, there is some dependence on the Froude number. However, the relation appears independent of the interstitial fluid.

The success in normalizing the velocity profiles for different bead sizes, Froude numbers, and interstitial fluids with the velocity at the surface of the flowing layer ($u_{surface}$) as shown in figure 6(*b*) suggests that the surface velocity is a key parameter of the flow. From table 1, we note that the surface velocity varies from $0.10\,\mathrm{m\,s^{-1}}$ to $0.77\,\mathrm{m\,s^{-1}}$ and increases with Froude number for all cases. The surface velocity decreases as the particles increase in size at a given Froude number. For small beads (1.2 mm and 2 mm), the surface velocity is higher for dry flow than for a water slurry, but the converse is true for large beads. The surface velocity is not strongly dependent on the interstitial fluid for the 3 mm beads.

The velocity at the surface of the layer can be estimated based on the shear rate. Assuming a simple linear velocity profile as a first-order approximation,

$$u_{surface} \approx \dot{\gamma}\dot{\delta}_0. \tag{8}$$

The theoretical relations for $\dot{\gamma}$ (equation (3)) and δ_0 (equation (7)) can be combined to predict the surface velocity as:

$$\left.\frac{u_{surface}}{\omega L}\right|_{theor} \approx \left(\frac{L}{d}\right)^{1/4} Fr^{-1/4}\left[\frac{\sin(\beta_m - \beta_s)}{\cos\beta_s}\right]^{1/4}. \tag{9}$$

Figure 7(*c*) suggests that the experimentally measured surface velocity approximately follows the scaling suggested by (9) for each Froude number. Again, the solid lines in figure 7(*c*) correspond to a least-squares fit for the data at each Froude number. Once

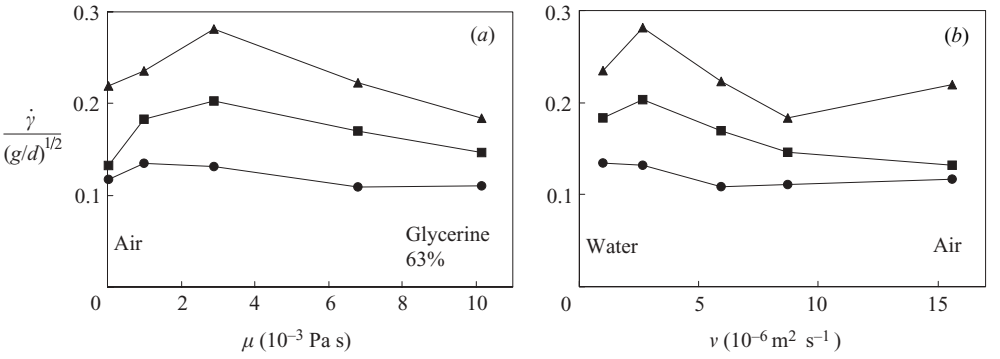

FIGURE 8. Dependence of dimensionless shear rate for 3 mm steel beads on (*a*) dynamic viscosity and (*b*) kinematic viscosity. Symbols: ●, $Fr = 0.39 \times 10^{-4}$; ■, $Fr = 1.26 \times 10^{-4}$; ▲, $Fr = 4.03 \times 10^{-4}$.

again, the data for each Froude number seem to fall on three nearly parallel lines, and the results are independent of the interstitial fluid at any given Froude number. However, it is also clear that the data does not collapse independent of the Froude number.

At this point, it is reasonable to consider more directly the effect of the interstitial fluid viscosity on the flow. To do this, we consider the shear rate in the flowing layer, since it is characteristic of the velocity profile, and it varies by nearly an order of magnitude, as indicated in table 1. In figure 8, we plot the shear rate as a function of both the dynamic viscosity, which reflects viscous friction effects, and the kinematic viscosity, which accounts for buoyancy effects in addition to viscous friction. It is apparent, based on purely dimensional arguments, that the dimensionless shear rate cannot be an explicit function of either the dynamic viscosity or the kinematic viscosity. However, this figure is included to indicate that the dynamics of the flowing granular layer are relatively independent of the interstitial fluid; the shear rate changes a surprisingly small amount over the wide range of interstitial fluid viscosities.

The number density profile of particles in the flowing layer is important for complete understanding of the flowing layer as well as for simulations and models of granular flow. Previous measurements in dry slurries indicate that the number density is near its maximum in the half of the layer near the fixed bed and drops off in the half of the layer nearest to the flowing surface (Ristow 1996; Jain *et al.* 2002). PIV images of the bead positions were used to determine the bead number density profile in the flowing layer. A rectangular window of length ~2.4 cm (0.17L or 800 pixels) perpendicular to the flowing surface and width 1 cm (350 pixels) along the flowing surface was used for the number density calculation. This window was divided into 20 bins perpendicular to the flowing surface, and the number of particles present in each bin was summed for the 99 image pairs.

The number density profiles for both the dry condition and the slurry condition are shown in figure 9(*a*). The data fall onto three distinct profiles, one for each bead size, for all interstitial fluids (air, water, and glycerine–water mixtures) and Froude numbers. For each of the larger beads, 2 mm and 3 mm in diameter, the number density profiles for different Froude numbers and interstitial fluids collapse, suggesting that number density profiles are dependent only on the bead size. For 1.2 mm beads, the number density profiles are independent of the Froude number, but the number density in the top half of the flowing layer is lower for the dry system

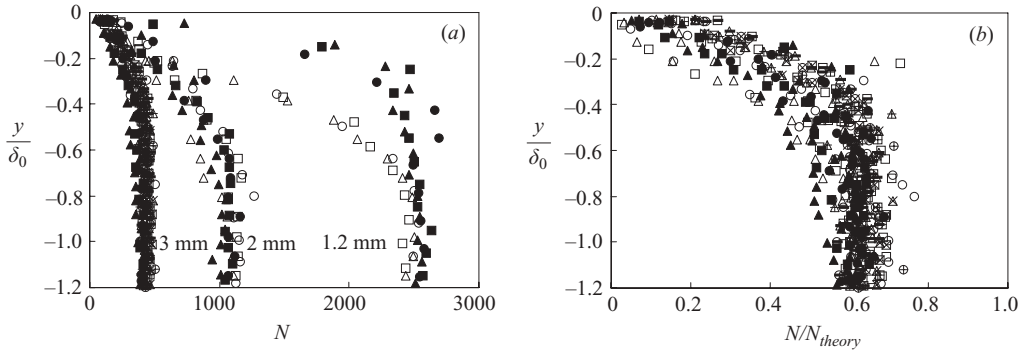

FIGURE 9. (*a*) Total number of beads counted in each bin as a function of depth in the flowing layer at $x = 0$. (*b*) Normalized number density profiles. Symbols: ●, $Fr = 0.39 \times 10^{-4}$; ■, $Fr = 1.26 \times 10^{-4}$; ▲, $Fr = 4.03 \times 10^{-4}$. Symbol fill: open, air; black, water; open with a '+' in the middle, 38% glycerine; open with a '×' in the middle, 56% glycerine; and open with a horizontal line, 63% glycerine.

than the number density in the corresponding region for the slurry system. This result may be related to the significantly higher surface velocity and shear rate for the 1.2 mm dry system compared to the slurry system, shown in figure 5(*c*). However, this higher surface velocity and shear only occur for the higher Froude numbers, while the lower Froude number dry system is similar to the slurry system in figure 5(*c*). This is different from the number density results in figure 9(*a*), where the dry system and slurry system each fall onto a different curve at all Froude numbers.

The profiles shown in figure 9(*a*) were calculated by simply counting the particles in bins distributed in the transverse direction from the flowing surface to the fixed bed. The number of beads of diameter d that could fit in a bin of area A if the flow is strictly two-dimensional is $N_{theory} = A/d^2$ for square packing. Although the granular flow is only quasi-two-dimensional, this theoretical value is useful to scale the number of beads as shown in figure 9(*b*) for all bead sizes, Froude numbers, and interstitial fluids. While the collapse is imperfect, it is clear that number density is near its maximum in the lower half of the flowing layer and drops off substantially in the top half of the layer approaching the surface of the flowing layer. The maximum number density in the lower half of the flowing layer and the fixed bead appears to be $N_{max} \approx 0.6\, N_{theory}$ independent of the interstitial fluid, which is slightly less than the value for glass beads in air (Jain *et al.* 2002).

The particle flux profile in the flowing layer can be obtained from the product of the velocity and the number density, as shown in figure 10. The mass flux is smallest at the top of the layer because of lower number density and near the fixed bed because of the low streamwise velocity. The mass flux is greatest for both dry and wet beads at about $y/\delta_0 = -0.4$, although the depth of the maximum varies from $y/\delta_0 = -0.2$ to $y/\delta_0 = -0.5$. Furthermore, the percentage of the average mass flux between $-0.25 \leqslant y/\delta_0 \leqslant 0$, $-0.75 \leqslant y/\delta_0 \leqslant -0.25$ and $-1 \leqslant y/\delta_0 \leqslant -0.75$ are 28% ($\pm 7\%$), 65% ($\pm 5\%$) and 8% ($\pm 3\%$), respectively (the percentages in the parentheses indicate one standard deviation in the measured mass flux). Thus, the bulk of the mass flow occurs in the middle portion of the flowing layer. Similar to our observation for the case of streamwise velocity profiles and number density profiles, most of the mass flux profiles corresponding to different bead diameters, Froude numbers, and interstitial fluids collapse on top of each other. The exception is the data for 1.2 mm

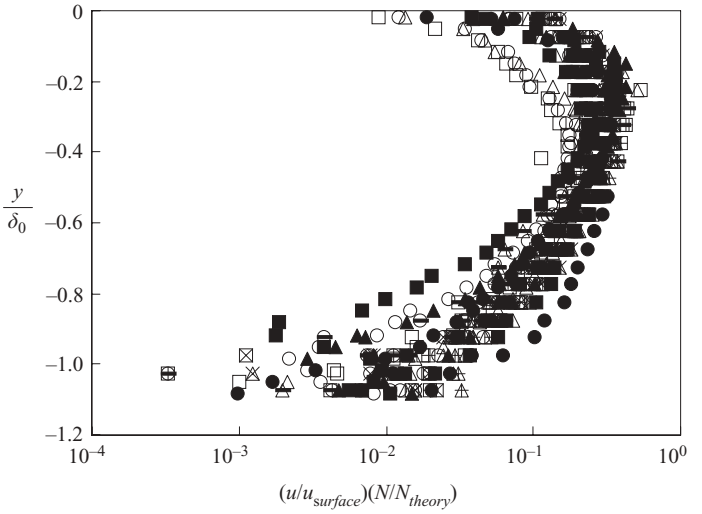

FIGURE 10. Mass flux profile at $x = 0$ for dry and wet beads. Symbols: ●, $Fr = 0.39 \times 10^{-4}$; ■, $Fr = 1.26 \times 10^{-4}$; ▲, $Fr = 4.03 \times 10^{-4}$. Symbol fill: open, air; black, water; open with a '+' in the middle, 38% glycerine; open with a '×' in the middle, 56% glycerine; and open with a horizontal line, 63% glycerine.

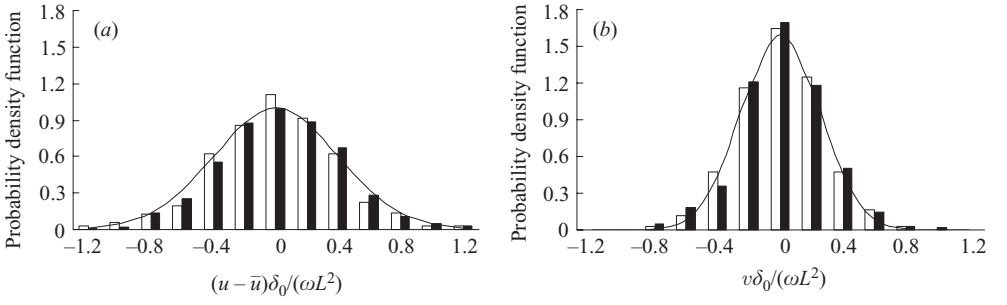

FIGURE 11. Probability density function (PDF) of the streamwise and transverse velocities for 2 mm steel beads near the top of the flowing layer ($-0.2 \leqslant y/\delta_0 \leqslant 0$) with air and water as the interstitial fluid. Symbols: white bars, air; black bars, water. The solid curve is a Gaussian distribution.

beads in air, which is related to the higher surface velocity and shear rate, as noted earlier.

One key difference between granular materials and fluids is that granular materials do not exhibit intrinsic thermal motion. Instead, velocity fluctuations, also known as the granular temperature, are generated by the flow itself (Menon & Durian 1997; Losert *et al.* 2000). As a result, the flow and velocity fluctuations are related. Of interest here is the effect of the interstitial fluid on the granular temperature. Figure 11 shows the probability density function (PDF) of the streamwise velocity and the transverse velocity near the surface of the flowing layer ($-0.2 \leqslant y/\delta_0 \leqslant 0$) for 2 mm beads at $Fr = 4.03 \times 10^{-4}$ with air and water as the interstitial fluid. The continuous curve represents a Gaussian distribution.

While there are some differences, the probability density function for both the streamwise and transverse velocities are similar for the two interstitial fluids. In

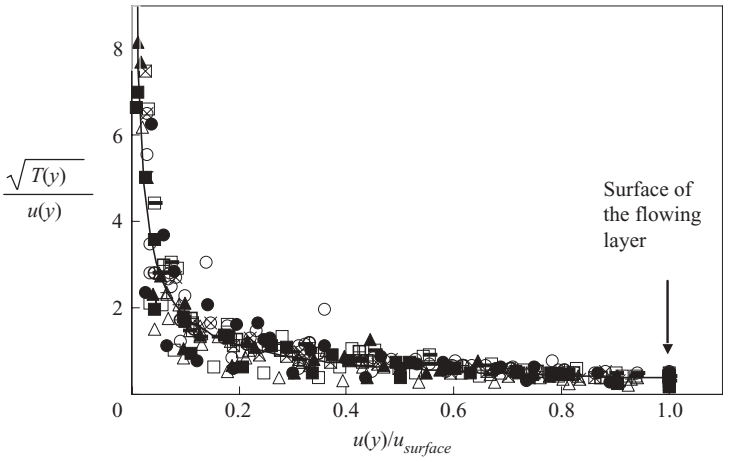

FIGURE 12. The granular temperature at $x = 0$ normalized by the local mean streamwise velocity, $u(y)$ is plotted against the dimensionless streamwise velocity. Symbols: ●, $Fr = 0.39 \times 10^{-4}$; ■, $Fr = 1.26 \times 10^{-4}$; ▲, $Fr = 4.03 \times 10^{-4}$. Symbol fill: open, air; black, water; open with a '+' in the middle, 38% glycerine; open with a '×' in the middle, 56% glycerine; and open with a horizontal line, 63% glycerine.

both cases, the distributions are essentially Gaussian. This is somewhat different from results for energetically vibrated systems in which the Gaussian distribution underestimates the probability of high and low velocity (Losert *et al.* 1999; Rouyer & Menon 2000). The streamwise and transverse probability density functions differ from each other in that the distribution of streamwise velocity is broader than that for the transverse velocity. This is simply a consequence of the streamwise velocity fluctuations being larger than the transverse velocity fluctuations. The ratio of transverse temperature to streamwise temperature for all experiments involving different bead sizes, Froude numbers, and interstitial fluids ranged from 0.56 to 0.68 across the flowing layer, with the smallest values in the middle of the layer.

To calculate the granular temperature through the flowing layer, the layer was divided into 10 bins along the transverse direction. For each of these 10 bins the granular temperature was calculated as (Hermann 1993; Goldhirsch 2003):

$$T = (\langle \boldsymbol{u}^2 \rangle - \langle \boldsymbol{u} \rangle^2), \tag{10}$$

where, $\boldsymbol{u}$ is the two-component velocity vector (streamwise and transverse velocities) and the angled brackets indicate a time average. The time between images of an image pair ($\sim 10^{-3}$ s) was less than the estimate for the time scale of particle collisions ($d/u \sim 10^{-2}$ s), so it is unlikely that the measured temperature was affected by multiple particle collisions taking place in the interval between the images. Figure 12 compares the granular temperature profiles for all bead sizes when the interstitial fluid is air, water, or mixtures of glycerine and water. In this figure, the square root of granular temperature normalized by local streamwise velocity is plotted against the normalized local streamwise velocity. A power-law relation between granular temperature and local streamwise velocity results, as indicated by the solid curve described by:

$$\frac{\sqrt{T(y)}}{u(y)} = 0.38 \left(\frac{u(y)}{u_{surface}} \right)^{-0.68}. \tag{11}$$

Based on this result, the granular temperature is 38% of the maximum streamwise velocity near the surface of the flowing layer. This is higher than the 8% or 2–4% values found previously by using MRI and optical probes, respectively (Boateng & Barr 1997; Caprihan & Seymour 2000), but consistent with our previous results for glass beads in air (Jain *et al.* 2002). Of course, the granular temperature is higher near the flowing surface (where the particle concentration is lower) and smaller near the fixed bed (where the particle concentration is greater), consistent with intuition and previous results (Walton & Braun 1986; Campbell 1990). Deep in the flowing layer at small values of $u(y)/u_{surface}$, the velocity fluctuations are quite small – about one-tenth of the free-stream velocity. However, this is a significantly larger fraction of the local streamwise velocity than near the flowing surface, at large values of $u(y)/u_{surface}$. The collapse of the data in figure 12 indicates that there is no significant dependence of granular temperature on the viscosity of the interstitial fluid or the diameter of beads over a wide range of Froude numbers when the granular temperature is normalized with the local streamwise velocity.

4. Conclusions

Knowledge of flow dynamics in the flowing layer of a quasi-two-dimensional geometry is helpful for the understanding of three-dimensional granular systems, scale-up studies (Ottino & Khakhar 2002), and for mixing and segregation models. In this work, we have explored the effect of interstitial fluid on the dynamics of the flowing layer in a quasi-two-dimensional rotating drum.

First, consider the results obtained. Our results show interesting differences (and similarities) in granular dynamics between the dry and slurry cases. The angle of repose and the flowing layer thickness are smaller in the dry system than in the slurry system for the same bead diameter at the same Froude number. The shear rate and surface velocity are greater in the dry system than the slurry system for the same bead diameter at the same Froude number. These differences are more pronounced for the beads of smaller sizes. Regardless, both systems follow similar scaling relations: (i) shear rate is inversely related to the square root of particle size; (ii) layer thickness increases with the square root of angular velocity and increases with the quarter power of the particle size; and (iii) surface velocity is related to $(L/d)^{1/4}Fr^{-1/4}$.

Two different scaling techniques were used to scale the streamwise velocity profiles. Scaling based on the mass balance works well for bigger beads, but for smaller beads the velocity profiles differ for the slurry system and the dry system. However, normalizing the streamwise velocity with the maximum velocity at the top of the flowing layer collapses the velocity profiles for bead sizes from 1.2 mm to 3 mm, Froude numbers from 0.39×10^{-4} to 4.0×10^{-4}, interstitial fluid densities from $1.184\,\mathrm{kg\,m^{-3}}$ to $1163\,\mathrm{kg\,m^{-3}}$, and interstitial fluid viscosities from 0.018×10^{-3} Pa s to 10.2×10^{-3} Pa s. The streamwise velocity profile is nearly linear in the upper three-quarters of the flowing layer ($y/\delta_0 > -0.75$) and the scaled streamwise velocity is approximately equal to $1 + 1.2(y/\delta_0)$. Near the interface between the layer and the fixed bed, the streamwise velocity logarithmically decreases to zero.

The number density profiles scaled using geometric arguments result in a reasonable collapse for different bead sizes, Froude numbers, and fluid properties. The number density changes dramatically in the upper half of the flowing layer, but remains nearly constant in the lower half of the flowing layer. A non-dimensionalization scheme based on a maximum packing density works well for 3 mm and 2 mm beads, but for

1.2 mm beads the number density in the top half of the layer is greater in the slurry case compared to the dry counterpart. Combining the streamwise velocity profiles with the number density profiles provides profiles of the mass flux. The maximum mass flux occurs at about 40% of the depth from the top surface to the fixed bed.

The magnitude of the velocity fluctuations decreases with depth in the flowing layer. Near the surface of the flowing layer, the fluctuations can be as large as 38% of the maximum streamwise velocity. The fluctuations decrease to less than one-tenth of the surface velocity near the fixed bed, but the fluctuations are much larger than the local streamwise velocity. The distribution of the transverse velocity fluctuations is similar in nature to that for the streamwise velocity fluctuations, although the r.m.s. value of transverse velocity fluctuations is about two-thirds that of the streamwise velocity fluctuations.

Of course, these measurements were made in a quasi-two-dimensional drum. In fact, the issue of selecting the axial dimension of the tumbler is a balancing act – if the gap is too wide, three-dimensional effects may play a role. While we expect that the effect of the sidewalls on the flow is not substantial, as described earlier, caution must be used in extending these results to three-dimensional systems. Nevertheless, we can make a few general observations. It is somewhat surprising that the scaling for the shear rate works well in the slurry case, because the reasoning behind equation (3) was built upon ideas of dry friction. It is known that adding a little liquid to a granular material produces substantial changes in its behaviour (Samadani & Kudrolli 2001; Li & McCarthy 2003; Tegzes *et al.* 2003). However, it is unexpected that if the particles are completely submerged in a liquid, the granular flow is very similar to that of dry granular materials. The results in this paper show that the physics may be similar. The similarities in behaviour between dry materials and slurries are due to the basis for the scaling relation, equation (3). The characteristic shear rate is essentially obtained by taking the characteristic length to be the particle diameter and the characteristic acceleration to be the net acceleration of particles (acceleration due to gravity minus the frictional force per unit mass). Since the correlation works, this suggests that there may be an effective coefficient of friction even in the case of slurries. It is not surprising, however, that the scaling is not as good for the layer thickness and the surface velocity because (i) the free surface and the bed-flowing layer boundary are both diffuse and thus there is some subjective element in their determination; and (ii) the velocity profile has a linear portion and a logarithmic portion, the relative sizes of which vary depending on the parameters; the scaling, however, is valid only for the linear part.

Although the results presented here are limited to a quasi-two-dimensional system with the accompanying limitations, they suggest that there may be deep commonalities in the physics of flowing granular materials and suspensions. Further exploration of the theoretical foundations and further experimentation may be highly profitable to both domains. In addition, it may be worth revisiting the original Bagnold experiments for liquid–solid suspension flows and how they can be applied to granular flows, as suggested by Hunt *et al.* (2002).

This work was funded by the Office of Basic Energy Sciences of the Department of Energy. We thank Professor Devang Khakhar from IIT Bombay for valuable comments and to Professor Edwin A. Cowen of Cornell University for providing the particle tracking velocimetry code. Nitin Jain acknowledges the support of his employer ZS Associates.

REFERENCES

Bagnold, R. A. 1954 Experiments on gravity free dispersion of large solid spheres in a Newtonian fluid under shear. *Proc. R. Soc. Lond.* A **225**, 49–63.

Baxter, G. W., Behringer, R. P., Fagert, T. & Johnson, G. A. 1989 Pattern-formation in flowing sand. *Phys. Rev. Lett.* **62**, 2825–2828.

Boateng, A. A. & Barr, P. V. 1997 Granular flow behaviour in the transverse plane of a partially filled rotating cylinder. *J. Fluid Mech.* **330**, 233–249.

Bonamy, D., Daviaud, F. & Laurent, L. 2002 Experimental study of granular flows via a fast camera: a continuous description. *Phys. Fluids* **14**, 1666–1673.

Boote, O. A. M. & Thomas, P. J. 1999 Effects of granular additives on transition boundaries between flow states of rimming flows. *Phys. Fluids* **11**, 2020–2029.

Bridgwater, J. 1976 Fundamental powder mixing mechanisms. *Powder Technol.* **15**, 215–236.

Campbell, C. S. 1990 Rapid granular flows. *Annu. Rev. Fluid Mech.* **22**, 57–92.

Caprihan, A. & Seymour, J. D. 2000 Correlation time and diffusion coefficient imaging: application to a granular flow system. *J. Magnet. Reson.* **144**, 96–107.

Carpen, I. C. & Brady, J. F. 2002 Gravitational instability in suspension flow. *J. Fluid Mech.* **472**, 201–210.

Coussot, P. & Ancey, C. 1999 Rheophysical classification of concentrated suspensions and granular pastes. *Phys. Rev.* E **59**, 4445–4457.

Cowen, E. A. & Monismith, S. G. 1997 A hybrid digital particle tracking velocimetry technique. *Exps. Fluids* **22**, 199–211.

DasGupta, S., Khakhar, D. V. & Bhatia, S. K. 1991 Axial segregation of particles in a horizontal rotating cylinder. *Chem. Engng Sci.* **46**, 1513–1517.

Duran, J. 2000 *Sands, Powders, and Grains.* Springer.

Dury, C. M. & Ristow, G. H. 1997 Radial segregation in a two-dimensional rotating drum. *J. Phys. I France* **7**, 737–745.

Dury, C. M., Ristow, G. H., Moss, J. L. & Nakagawa, M. 1998 Boundary effects on the angle of repose in rotating cylinders. *Phys. Rev.* E **57**, 4491–4497.

Felix, G., Falk, V. & D'Ortona, U. 2002 Segregation of dry granular material in rotating drum: experimental study of the flowing zone thickness. *Powder Technol.* **128**, 314–319.

Fiedor, S. J. & Ottino, J. M. 2003 Dynamics of segregation and coarsening of granular materials and slurries in circular and square cylinders. *Phys. Rev. Lett.* **91**, 244 301.

Goldhirsch, I. 2003 Rapid granular flows. *Annu. Rev. Fluid Mech.* **35**, 267–293.

Haff, P. H. 1983 Grain flow and a fluid-mechanical phenomenon. *J. Fluid Mech.* **134**, 401–430.

Harwood, C. F. 1977 Powder segregation due to vibration. *Powder Technol.* **16**, 51.

Henein, H., Brimacombe, J. K. & Watkinson, A. P. 1983 Experimental study of transverse bed motions in rotary kilns. *Metal. Trans.* B **14**, 191–205.

Hermann, H. J. 1993 On the thermodynamics of granular media. *J. Phys. II France* **3**, 427–433.

Heywood, N. I. 1999 Stop your slurries from stirring up trouble. *Chem. Engng Prog.* **95**, 21–41.

Hill, K. M. & Kakalios, J. 1994 Reversible axial segregation of binary-mixtures of granular-materials. *Phys. Rev.* E **49**, 3610–3613.

Hunt, M. L., Zenit, R., Campbell, C. S. & Brennen, C. E. 2002 Revisiting the 1954 suspension experiments of R. A. Bagnold. *J. Fluid Mech.* **452**, 1–24.

Jain, N., Khakhar, D. V., Lueptow, R. M. & Ottino, J. M. 2001 Self-organization in granular slurries. *Phys. Rev. Lett.* **86**, 3771–3774.

Jain, N., Ottino, J. M. & Lueptow, R. M. 2002 Velocity of flowing granular layer in a rotating tumbler. *Phys. Fluids* **14**, 572–582.

Khakhar, D. V., Orpe, A. V., Andersen, P. & Ottino, J. M. 2001*b* Surface flow of granular materials: model and experiments in heap formation. *J. Fluid Mech.* **441**, 255–264.

Khakhar, D. V., Orpe, A. V. & Ottino, J. M. 2001*a* Surface granular flows: two related examples. *Adv. Complex Systems* **4**, 407–417.

Klein, S. P. & White, B. R. 1988 Dynamic shear of granular material under variable gravity conditions. *Am. Inst. Aeronaut. Astronaut.* **88**, 1–10.

Komatsu, T. S., Inagaki, S., Nakagawa, N. & Nasuno, S. 2001 Creep motion in a granular pile exhibiting steady state surface flows. *Phys. Rev. Lett.* **86**, 1757–1760.

Lacey, P. M. 1954 Developments in the theory of particle mixing. *J. Appl. Chem.* **4**, 257–268.

Li, H. & McCarthy, J. J. 2003 Controlling cohesive particle mixing and segregation. *Phys. Rev. Lett*. **90**, 184 301.

Losert, W., Bocquet, L., Lubensky, T. C. & Gollub, J. P. 2000 Particle dynamics in sheared granular matter. *Phys. Rev. Lett*. **85**, 1428–1431.

Losert, W., Cooper, D. G. W., Delour, J., Kudrolli, A. & Gollub, J. P. 1999 Velocity statistics in excited granular media. *Chaos* **9**, 682–690.

Lueptow, R. M., Akonur, A. & Shinbrot, T. 2000 PIV for granular flows. *Exp. Fluids* **28**, 183–186.

Medina, A., Córdova, J. A., Luna, E. & Treviño, C. 1998 Velocity field measurements in granular gravity flow in a near 2D silo. *Phys. Lett*. A **250**, 111–116.

Medved, M., Jaeger, H. M. & Nagel, S. R. 2001 Convection in a fully immersed granular slurry. *Phys. Rev*. E **63**, 061 302.

Menon, N. & Durian, D. J. 1997 Diffusing-wave spectroscopy of dynamics in a three-dimensional granular flow. *Science* **275**, 1920–1922.

Nakagawa, M., Altobelli, S. A., Caprihan, A., Fukushima, E. & Jeong, E. K. 1993 Non-invasive measurements of granular flows by magnetic resonance imaging. *Exps. Fluids* **16**, 54–60.

Orpe, A. V. & Khakhar, D. V. 2001 Scaling relations for granular flow in quasi-2d rotating cylinder. *Phys. Rev*. E **64**, 1302.

Ottino, J. M. & Khakhar, D. V. 2002 Scaling of granular flow processes: from surface flows to design rules. *AIChE J*. **48**, 2157–2166.

Rajchenbach, J. 1990 Flow in powders: from discrete avalanches to continuous regime. *Phys. Rev. Lett*. **65**, 2221–2224.

Reynolds, O. 1885 On the dilatancy of media composed of rigid particles in contact. *Phil. Mag*. (5) **50**, 469.

Ristow, G. H. 1996 Dynamics of granular materials in a rotating drum. *Europhys. Lett*. **34**, 263–268.

Ristow, G. H. 2000 *Pattern Formation in Granular Materials*. Springer.

Rouyer, F. & Menon, N. 2000 Velocity fluctuations in a homogeneous 2D granular gas in steady state. *Phys. Rev. Lett*. **85**, 3676–3679.

Samadani, A. & Kudrolli, A. 2001 Angle of repose and segregation in cohesive granular matter. *Phys. Rev*. E **64**, 051 301.

Schleier-Smith, J. M. & Stone, H. A. 2001 Convection, heaping, and cracking in vertically vibrated granular slurries. *Phys. Rev. Lett*. **86**, 3016–3019.

Takahashi, H., Suzuki, A. & Tanaka, T. 1968 Behaviour of a particle bed in the field of vibration – Analysis of particle motion in a vibrating vessel. *Powder Technol*. **2**, 65.

Tegzes, P., Vicsek, T. & Schiffer, P. 2003 Development of correlations in the dynamics of wet granular avalanches. *Phys. Rev*. E **67**, 051 303.

Tirumkudulu, M., Tripathi, A. & Acrivos, A. 1999 Particle segregation in monodisperse sheared suspensions. *Phys. Fluids* **11**, 507–509.

Walton, O. R. & Braun, R. L. 1986 Stress calculations for assemblies of inelastic spheres in uniform shear. *Acta Mech*. **63**, 73–86.

Warr, S., Jacques, G. T. H. & Huntley, J. M. 1994 Tracking the translational and rotational motion of granular particles: use of high-speed photography and image processing. *Powder Technol*. **81**, 41–56.

Williams, J. C. 1963 The segregation of powders and granular materials. *Fuel Soc. J*. **14**, 29–34.